

Superstructure of Mullite-type $\text{KAl}_9\text{O}_{14}$

Biljana Lazic,^{*,†} Hannes Krüger,^{‡,||} Reinhard Kaindl,^{‡,§} Lukas Perfler,[‡] Aleksandar Kremenović,[⊥] Vladica Cvetković,[⊥] and Ray L. Withers^{||}

[†]Mineralogical Crystallography, Institute of Geological Sciences, University of Bern, Freiestrasse 3, 3012 Bern, Switzerland

[‡]Institute of Mineralogy and Petrography, University of Innsbruck, Innrain 52, 6020 Innsbruck, Austria

[§]Institute for Surface Technologies and Photonics, Functional Surfaces, Joanneum Research Forschungsgesellschaft mbH, Leobner Strasse 94, 8712 Niklasdorf, Austria

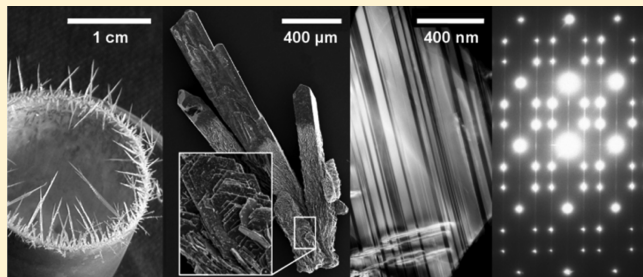
^{||}Research School of Chemistry, Australian National University, Canberra, ACT 0200, Australia

[⊥]Faculty of Mining and Geology, Laboratory for Crystallography, University of Belgrade, Džusina 7, 11000 Belgrade, Serbia

Supporting Information

ABSTRACT: Large whiskers of a new $\text{KAl}_9\text{O}_{14}$ polymorph with mullite-type structure were synthesized. The chemical composition of the crystals was confirmed by energy-dispersive X-ray spectroscopy, and the structure was determined using single-crystal X-ray diffraction. Nanosized twin domains and one-dimensional diffuse scattering were observed utilizing transmission electron microscopy. The compound crystallizes in space group $P2_1/n$ ($a = 8.1880(8)$, $b = 7.6760(7)$, $c = 8.7944(9)$ Å, $\beta = 110.570(8)^\circ$, $V = 517.50(9)$ Å³, $Z = 2$). Crystals of $\text{KAl}_9\text{O}_{14}$ exhibit a mullite-type structure with linear edge-sharing AlO_6 octahedral chains connected with groups of two AlO_4 tetrahedra and one AlO_5 trigonal bipyramidal. Additionally, disproportionation of $\text{KAl}_9\text{O}_{14}$ into $\text{K}\beta$ -alumina and corundum was observed using *in situ* high-temperature optical microscopy and Raman spectroscopy.

KEYWORDS: whiskers, mullite-type, superstructure, diffuse scattering, stacking faults



INTRODUCTION

Mullite is an important ceramic material, with excellent thermal and mechanical properties, such as high-temperature stability, strength and creep resistance, as well as a low dielectric constant and high electrical insulation capabilities. For more details and examples on properties and applications, see Schneider et al.¹

The chemical composition of mullites sensu stricto is given by the general formula $\text{Al}_2(\text{Al}_{2+2x}\text{Si}_{2-2x})\text{O}_{10-x}$. The amount of Si^{4+} substituted by Al^{3+} is correlated with the sum of oxygen vacancies necessary to retain charge balance. Some specific mullites compositionally between sillimanite and $\text{i-Al}_2\text{O}_3$ are summarized by Fischer et al.² Apart from the “true” mullites, structurally related mullite-type materials exist. To be classified as mullite-type, a material has to crystallize in a subgroup of $P4/mbm$ (the space group of the mullite aristotype) and has to exhibit a characteristic (pseudo-) orthogonal arrangement of edge-sharing MO_6 octahedra.³

In mullite-type aluminates $\text{M}^{+2-2x}\text{Al}_2(\text{Al}_4)\text{O}_{10-x}$, negative charge is compensated by incorporation of an equivalent number ($2-2x$) of monovalent M cations.⁴ Using this equation, the subject of this study $\text{KAl}_9\text{O}_{14}$ can be expressed as $\text{K}_{0.67}\text{Al}_2(\text{Al}_4)\text{O}_{9.33}$. The chemical composition of this kind of aluminate can be split into compositionally invariant chains of octahedra Al_2O_8 and a residue with variable composition and

configuration $\text{M}^{+2-2x}(\text{Al}_4)\text{O}_{2-x}$. The arrangement of edge-sharing octahedral chains, running parallel to the c -direction, is a characteristic structural feature of all mullites and mullite-type materials. Differences in symmetry and composition can be created by ordering of the oxygen vacancies and accompanying cations in the variable part of the structure, the part connecting the octahedral chains. Thus, this variable part of the overall structure is usually the source of the structural modulations or disorder characteristic of mullites.

The investigations of mullite-type alkali aluminates were mainly related to the study of different phase compositions: $\text{Na}_2\text{O}-\text{Al}_2\text{O}_3$,^{5,6} $(\text{Na}, \text{K})_2\text{O}-\text{BaO}-\text{Al}_2\text{O}_3$,^{5,7} $\text{Al}_2\text{O}_3-\text{B}_2\text{O}_3$, and $\text{Al}_2\text{O}_3-\text{K}_2\text{O}$.⁶ A new phase $\lambda\text{-Na}_2\text{O}\cdot x\text{Al}_2\text{O}_3$, exhibiting a wide compositional variation ($3 \leq x \leq 12$), was discovered by Elliot and Huggins.⁷ This compound shows typical “mullite” lattice parameters $a = 7.58$, $b = 7.68$, and $c = 2.88$ Å. Mazza et al.⁶ were able to index the powder diagrams of five boron-containing samples with a composition of $\text{Al}_{6-x}\text{B}_x\text{O}_9$ ($1 \leq x \leq 3$) and two mullite-type alkali aluminates, reported as $\text{NaAl}_6\text{O}_{9.5}$ and $\text{KAl}_6\text{O}_{9.5}$ using a pseudotetragonal unit cell of $a \cong b \cong 7.640$ Å and $c \cong 2.937$ Å and $a \cong b \cong 7.708$ Å and $c \cong 2.906$ Å,

Received: November 28, 2012

Revised: January 19, 2013

Published: January 22, 2013

respectively. Fischer et al.⁴ studied the solid solution series between the mullite-type K and Na end-members, determined the cation positions, and reported corrected compositions of $\text{Na}_{0.67}\text{Al}_6\text{O}_{9.33}$ and $\text{K}_{0.67}\text{Al}_6\text{O}_{9.33}$. Angerer⁹ investigated the behavior of these phases at high temperatures and reported the dissociation of $\text{K}_{0.67}\text{Al}_6\text{O}_{9.5}$ into potassium β -alumina and Al_2O_3 above 1273 K. Mazza et al.,⁸ Fischer et al.,⁴ and Angerer⁹ used a nitrate decomposition method for the synthesis of the precursor. As reported by Fischer et al.,⁴ the final products were multiphase nano- to microcrystalline materials, from which the exact chemical composition could not be determined.

We found a method to synthesize large whiskers of $\text{KAl}_9\text{O}_{14}$. The characterization of the crystals was performed using X-ray diffraction (XRD), transmission electron microscopy (TEM), high temperature (HT) optical microscopy, and Raman spectroscopy.

EXPERIMENTAL SECTION

Whiskers of $\text{KAl}_9\text{O}_{14}$ have been observed as byproducts of a crystal growth experiment using K_3AlF_6 flux. To exclude any effects of the nutrient, the experiment was repeated using only K_3AlF_6 as starting material. Powdered K_3AlF_6 was placed in an open Pt-crucible and heated in air to 1273 K. This temperature was held for 1 h. Subsequently, the material was cooled to 473 K at a rate of 10 K/h. Long prismatic colorless needles of $\text{KAl}_9\text{O}_{14}$ were found at the rim of the Pt-crucible, some as long as 1 cm (Figure 1).

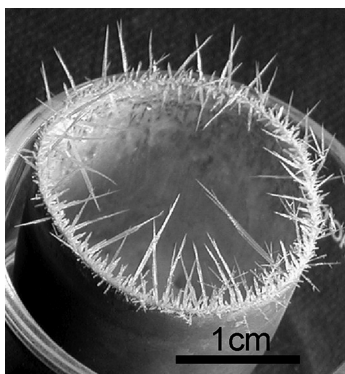


Figure 1. Crystals of $\text{KAl}_9\text{O}_{14}$ grown at the rim of a Pt crucible.

To perform electron microprobe analyses (EMPA), crystals were embedded in resin, polished, and carbon coated. The analysis was performed using a JEOL JSM-6610LV scanning electron microscope (SEM) connected with an INCA35 energy dispersive X-ray analysis (EDX) unit. An acceleration voltage of 20 kV was used. The following standards were employed: Al_2O_3 , SiO_2 , and MAD-10 orthoclase for K.

For X-ray diffraction experiments, a small crystal of good optical quality and without any visible twinning was mounted on the tip of a glass fiber. Diffraction data were collected at ambient conditions using a STOE IPDS-II imaging plate diffractometer. The parameters of the data collection are summarized in Table 1. An analytical absorption correction based on 13 indexed faces was applied. The data reduction including Lorentz and polarization correction was performed with the Stoe X-Area¹⁰ software. The crystal structure of $\text{KAl}_9\text{O}_{14}$ was solved by direct methods using Sir97¹¹ and refined using Jana2006.¹²

For electron microscopy analysis, selected single crystals were powdered in an agate mortar, and finally dispersed on a holey carbon film using ethanol. Microscopy was performed using a Philips EM430 operated at 300 kV. Images were recorded on large format sheet film.

To study the thermal behavior of $\text{KAl}_9\text{O}_{14}$, *in situ* high-temperature XRD experiments were performed on a STOE IPDS-II diffractometer system, equipped with a STOE Heatstream attachment. The crystal was embedded in a 0.1 mm SiO_2 glass capillary. Data collections were

Table 1. Data Collection and Structure Refinement of $\text{KAl}_9\text{O}_{14}$

crystal size	0.06 × 0.18 × 0.38 mm
space group	$P2_1/n$ (No. 14)
unit cell dimensions	$a = 8.1880(8)$ Å
	$b = 7.6760(7)$ Å
	$c = 8.7944(9)$ Å
	$\beta = 110.570(8)^\circ$
volume	517.50(9) Å ³
Z	2
density (calcd)	3.248 g/cm ³
abs coeff	1.380 mm ⁻¹
F(000)	496
diffractometer	STOE IPDS II
X-ray radiation	Mo K α
temp	298 K
scan mode	ω -scan
no. of frames	180
time per frame	20 min/frame
θ range	2.92–26.97°
index ranges	$-10 \leq h \leq 10$ $-9 \leq k \leq 9$ $-11 \leq l \leq 11$
reflns collected	6360
ind reflns	2652 ($R_{\text{int}} = 0.0560$)
max/min transmission	0.9654/0.8621
structure solution	Sir97 ¹¹
refinement method	full-matrix least-squares on F
refinement program	Jana2006 ¹²
data/restraints/parameters	2652/0/114
GOF	2.830
$\Delta/\sigma_{\text{max}}$	0.007
R for 2416 data, $I > 2\sigma(I)$	$R = 0.0296$, $wR2 = 0.0395$
R for all data	$R = 0.0330$, $wR2 = 0.0400$
weighting scheme	$w = 1/(\sigma^2(F) + 0.0001F^2)$
residual electron density	0.34/−0.57

carried out up to 1083 K. Temperature calibration was achieved by the procedure described by Krüger and Breil.¹³ For further investigations above 1083 K, HT optical microscopy was used. One of the crystals was heated on an Olympus BX40 microscope equipped with a Linkam TS1500 high-temperature stage. The temperature of the stage was controlled by a TMS94 controller using an S-type thermocouple. The crystal was placed on a sapphire plate and heated (in air) to 1473 K at a rate of 100 K/min. Images were recorded every 30 s with a PixeLINK PL-A662 FireWire Camera attached to the microscope. From 1473 to 1623 K, the crystal was heated at a rate of 5 K/min and images were recorded every 10 s.

Confocal Raman spectra of the single crystals over the range of 100–4000 cm⁻¹ were recorded with a Horiba Jobin Yvon Labram-HR 800 Raman microspectrometer. The samples were excited using the 532 nm emission line of a frequency-doubled 100 mW Nd:YAG laser under an Olympus 100× objective lens (numerical aperture 0.9). The size of the laser spot on the surface was approximately 1 μm .

The scattered light was dispersed by an optical grating with 1800 lines mm⁻¹ and collected by a 1024 × 256 open electrode CCD detector. The spectral resolution, determined by measuring the Rayleigh line, was about 2 cm⁻¹. The spectra were recorded unpolarized. Second-order polynomial and convoluted Gaussian–Lorentzian functions were fitted to the background and Raman bands, respectively, using the built-in spectrometer software LabSpec.¹⁴ The accuracy of the Raman line shifts, calibrated by Neon spectral calibration lamp, was on the order of 0.5 cm⁻¹. Raman spectra were measured on $\text{KAl}_9\text{O}_{14}$ whiskers at ambient conditions and thermally treated crystals as well as on pure K β -alumina crystals.

RESULTS

The preliminary investigation of the synthesized $\text{KAl}_9\text{O}_{14}$ crystals was performed using a petrographic microscope. In cross-polarized light, most of the crystals show lamellar twinning perpendicular to the needle axis as presented in Figure 2. This type of pseudotetragonal twinning was also observed in some crystals by single-crystal XRD.

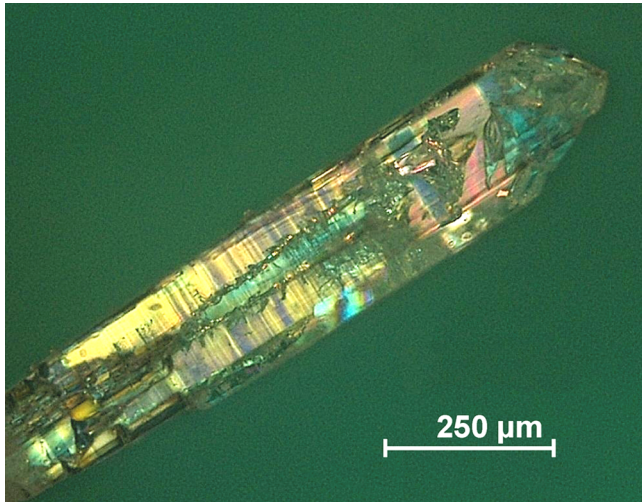


Figure 2. Crystal of $\text{KAl}_9\text{O}_{14}$ in cross-polarized light, showing lamellar twinning perpendicular to the needle axis.

The microprobe analysis showed that the composition of the crystals is consistent with the stoichiometric formula $\text{KAl}_9\text{O}_{14}$. A second type of crystal was found among the synthesis products (small hexagonal plates, as visible at the root of the $\text{KAl}_9\text{O}_{14}$ needles in Figure 3). These were identified, by means of single-crystal XRD, as $\text{K}\beta$ -alumina, a nonstoichiometric compound with the composition $\text{K}_{2.6}\text{Al}_{21.86}\text{O}_{34}$.¹⁵

First attempts to index the X-ray diffraction pattern of the $\text{KAl}_9\text{O}_{14}$ crystals revealed an orthorhombic $3 \times 1 \times 3$ supercell of the cell published by Fischer et al.⁴ However, this supercell is simulated by partial-merohedral twinning. In fact, the real cell is monoclinic and related to the known orthorhombic cell⁴ by the

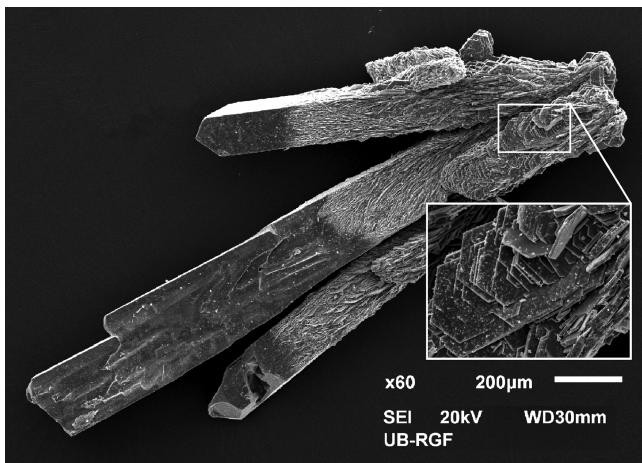


Figure 3. SEI (secondary electron imaging) of $\text{KAl}_9\text{O}_{14}$ crystals. Hexagonal crystals of $\text{K}\beta$ -alumina, grown on the surface of $\text{KAl}_9\text{O}_{14}$ whiskers.

following transformation: $a_{\text{mon}} = a_{\text{or}} - c_{\text{or}}$, $b_{\text{mon}} = b_{\text{or}}$, $c_{\text{mon}} = 3c_{\text{or}}$. The geometric relation between the cells in reciprocal space is shown in Figure 4. The twin individuals are related by a

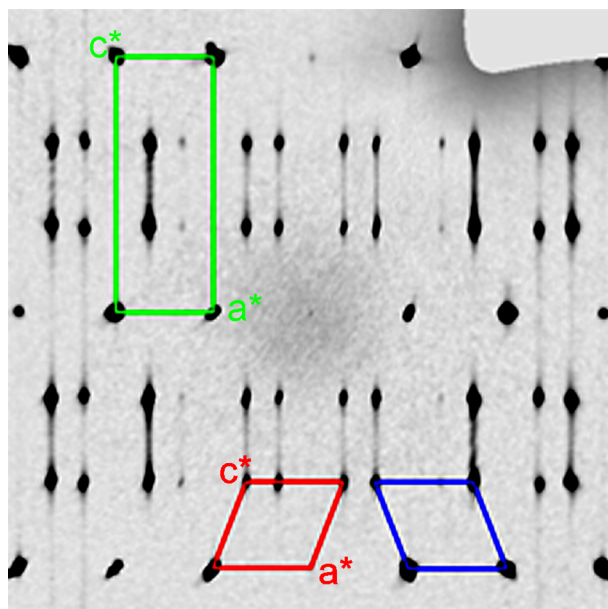


Figure 4. ($h1l$) layer of the reciprocal space of $\text{KAl}_9\text{O}_{14}$. The unit cell of the known orthorhombic polymorph⁴ (green) and two twin-related monoclinic unit cells (red/blue) are shown.

2-fold rotation axis along a^* . As a result, the reciprocal lattices show overlap for all lattice nodes with $l = 3n$. All nodes with $l \neq 3n$ are fully separated.

As the lattices do not overlap perfectly (see below), refinement of the lattice parameters was done using reflections from one twin domain only, rejecting all overlapped lattice nodes ($l = 3n$). The structure was solved by direct methods in space group $P2_1/n$, using data from one domain only. The structure refinement revealed a ratio of the twin volumes of 44/56, with an R -value of 5.5%. Careful analysis of the “not matching” reflections showed that reflections with $l \neq 3n$ had negative $F_o - F_c$ differences, whereas $l = 3n$ reflections showed $(F_o - F_c) > 0$. To account for the possible presence of orthorhombic domains, we utilized a second scaling factor for the $l = 3n$ reflections, to account for this effect. This improved the R -value to 3.1%. The additional intensity of the $l = 3n$ reflections originates from disordered regions, as will be discussed below. Atomic coordinates, equivalent isotropic and anisotropic displacement factors, as well as selected interatomic distances and angles are presented in Tables 2–4 in the Supporting Information.

The obtained electron diffraction (ED) patterns (Figure 5a) clearly show that the twinning does not produce exactly overlapping lattices: a small angular mismatch results in splitting of the reflections at higher diffraction angles and the obvious trapezium-shape arrangement of the superstructure reflections.

The same effect is visible in the X-ray data at very high diffracting angles. One-dimensional diffuse scattering is visible in the X-ray data (Figure 4), as well as in ED patterns (Figure 5b). The direction of the streaking is parallel to $3c_{\text{mon}}^* - a_{\text{mon}}^*$. Bright-field images along zone axis [010] (Figure 5c) show nanosized (5–100 nm) twin domains. A close inspection of the

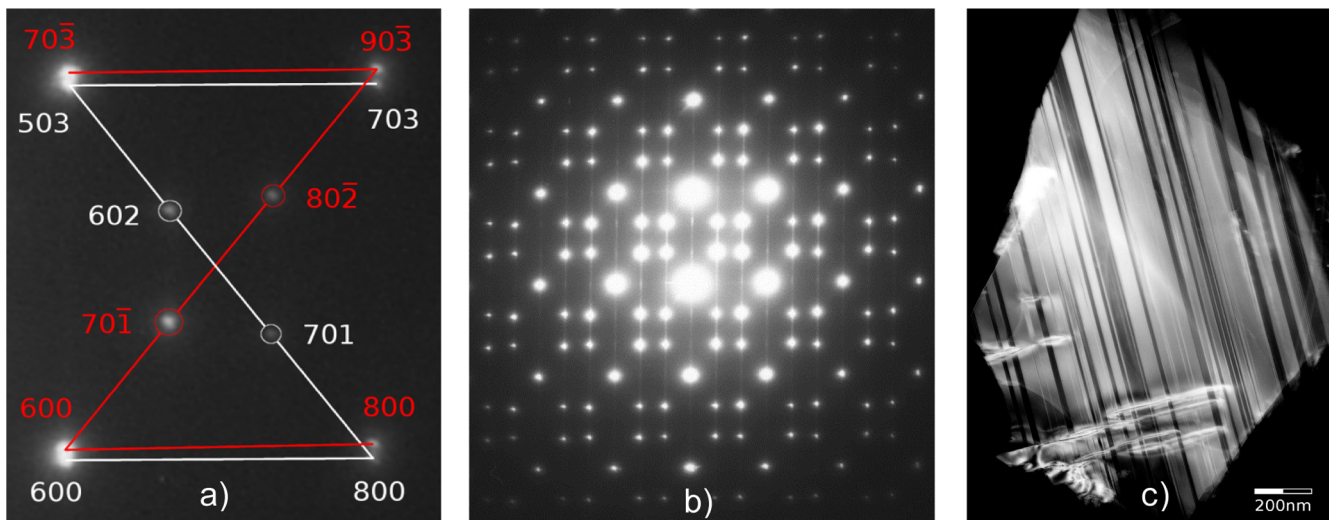


Figure 5. Transmission electron microscopy of $\text{KAl}_9\text{O}_{14}$: (a) indexed electron diffraction pattern, zone axis $[010]$ showing twinning by partial merohedry; characteristic trapezoidal arrangement of the superstructure reflections and splitting of “overlapped” main reflections; (b) one-dimensional diffuse scattering parallel to $c^* - (a^*/3)$; and (c) bright-field image, zone axis $[010]$ showing nanosized twin domains.

images reveals domains with three different contrasts, an indication that a third type of domain is present.

In situ single-crystal high-temperature XRD experiments on $\text{KAl}_9\text{O}_{14}$ detected no phase transition up to 1083 K. The lattice parameters at this temperature were determined to $a = 8.216(2)$, $b = 7.711(1)$, $c = 8.860(2)$ Å, $\beta = 110.62(1)^\circ$, and $V = 525.4(2)$ Å³. To continue the investigation at higher temperatures, we employed HT optical microscopy. No optical changes of the crystal were noticed up to 1573 K. At ca. 1573 K, the crystal started to alternate: formerly clear transparent domains became blurry, and recrystallization started from the edges and moved inward. At a temperature of 1588 K, the crystal was completely recrystallized, although the external shape was entirely preserved (Figure 6).

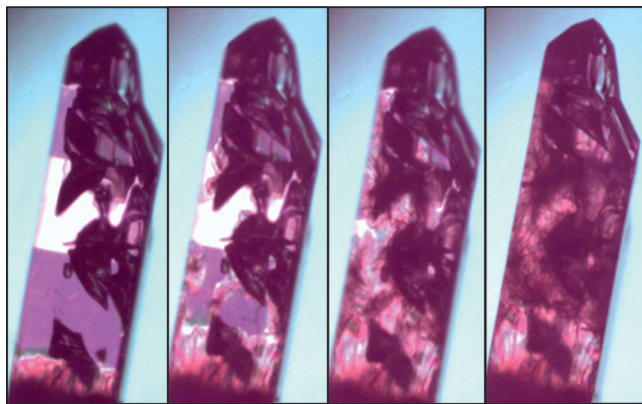


Figure 6. Photographs of a $\text{KAl}_9\text{O}_{14}$ crystal taken at 1573, 1577, 1581, and 1588 K.

After the HT-experiment, the crystal was cooled and investigated using Raman spectroscopy. The first spectrum, presented in Figure 7, was measured from a $\text{KAl}_9\text{O}_{14}$ whisker at ambient conditions, before high-temperature treatment. Raman measurements obtained from a $\text{KAl}_9\text{O}_{14}$ crystal after the HT optical microscopy showed that two distinct spectra [Figure 8, spectra (1) and (2)] can be found. The two spectra measured on the heat-treated $\text{KAl}_9\text{O}_{14}$ can be explained as a combination

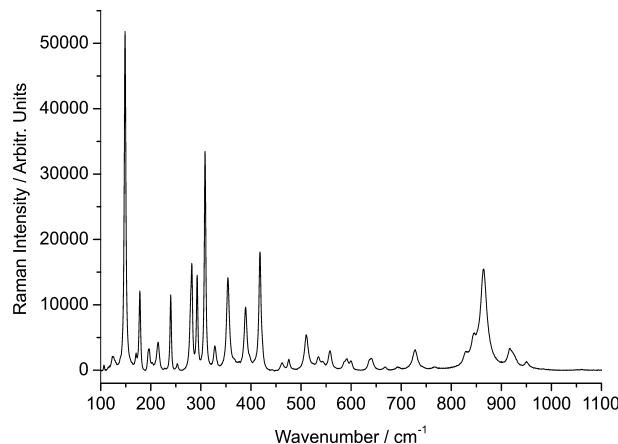


Figure 7. Unpolarized Raman spectra of $\text{KAl}_9\text{O}_{14}$.

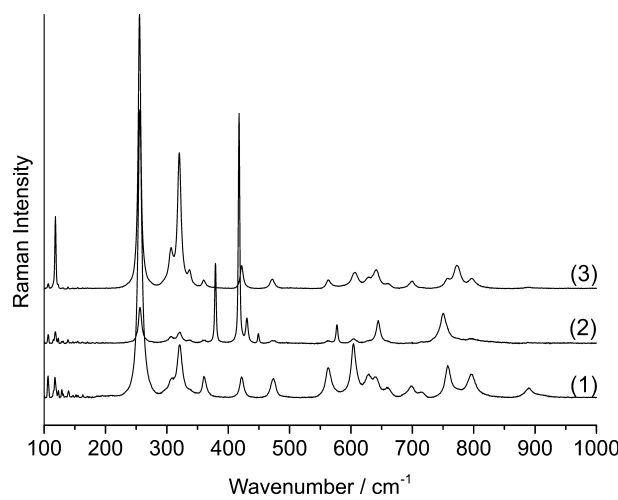


Figure 8. Raman spectrum of pure $\text{K}\beta$ -alumina (3) and two spectra obtained from $\text{KAl}_9\text{O}_{14}$ after temperature treatment: (1) spectra of $\text{K}\beta$ -alumina with a small amount of corundum, and (2) spectrum of corundum with minor amounts of $\text{K}\beta$ -alumina.

of the spectra of corundum and K β -alumina, in different ratios. As the Raman spectrum of K β -alumina was unknown, we measured it from pure K β -alumina crystals, which we checked beforehand by single crystal XRD. The spectrum is presented in Figure 8 (3). The Raman-active modes at 379 (Eg), 418 (A1g), 431 (Eg), 449 (Eg), 578 (Eg), 644 (A1g), and 751 cm $^{-1}$ (Eg), which are related to the [AlO₆] vibration modes, are particularly visible in spectrum (2), and they are characteristic for corundum.¹⁶ The additional bands at 256, 307, 321, 337, 360, 472, 564, 604, and 795 cm $^{-1}$ can be assigned to K β -alumina. This proves that KAl₉O₁₄ disproportionates into K β -alumina and corundum. In the Supporting Information, the Raman spectra of pure KAl₉O₁₄ and K β -alumina are provided.

Structure. The structure of monoclinic KAl₉O₁₄ exhibits all of the features of a typical mullite-type compound (Figure 9a).¹⁷ The main building units are chains of edge-sharing AlO₆ octahedral, which run parallel to the c-axis. They are linked by inner-chain groups comprising two AlO₄ tetrahedra and one AlO₅ trigonal bipyramidal. In Figure 9a–c, we draw the Al₅ coordination polyhedra as tetrahedra, with the fifth bond sticking out as a straight line. In the octahedral chains, Al1O₆ and Al2O₆ (Figure 9b) occur in a periodic sequence of Al1–Al1–Al2. The sequence of Al1 and Al2 atoms along the chains at the unit cell edges is related to the central chain by a translation vector of (1/2, 1/2, 1/2). The Al1O₆ is distorted having six distinct bonds varying between 1.8847(19) and 1.9590(16) Å.¹⁷ In contrast, Al2O₆ has almost perfect octahedral coordination, with nearly equal 3 × 2 bonds (O4 1.9163(15), O2 1.9240(12), and O6 1.9363(17) Å). Differences in geometry of these two octahedra can be expressed with (λ) quadratic elongation and (σ^2) bond angle variance.¹⁸ The values of these parameters are 1.0162(8)/54.0(2) for Al1O₆ and 1.0104(7)/36.9(2) for Al2O₆. In the inner-chain group, both tetrahedra Al3O₄ and Al4O₄ are linked via three oxygen atoms to the octahedral chains, and via the fourth oxygen atom (O7 in this work, Oc* in Fischer et al.⁴) to the Al5O₅ trigonal bipyramidal. This Al5O₅ polyhedron shows a typical 4 + 1 coordination, with four shorter (1.7569(16)–1.8625(14) Å) and one significantly longer bond (2.1612(13) Å), which still contributes ca. 8% to the total bond valence sum. The three shortest bonds connect the Al₅ atom to the octahedral chains and via a fourth, slightly longer 1.8625(14) Å bond (Al₅–O7) to the two tetrahedra (Figure 9c, Table 4 in the Supporting Information). The fifth, longer bond connects to O5. The K atoms are located in the center of the cavities between the Al1O₆, Al2O₆, and Al5O₅ polyhedra, exhibiting six shorter (2.8456(17)–2.8748(15) Å) and two longer bonds (2.9585(13) Å) to their oxygen atoms. The nearly planar arrangement of these bonds affects the anisotropic displacement parameters of the K, which thus takes the form of a strongly elongated ellipsoid (Figure 9c).

DISCUSSION

Mullite needles, fibers, and whiskers have attracted significant attention as reinforcement material for metal and ceramic composites, enhancing their mechanical and thermal properties.^{3,19} Methods for their synthesis are usually classified into solid-state, hydrothermal, and vapor-state processes. The flux method was reported as reliable for synthesis of uniform crystals.²⁰ However, the synthesis of 1 cm long KAl₉O₁₄ whiskers was not expected in a synthesis using a K₃AlF₆ flux. As the crystals were found at the rim of the crucible (ca. 2 cm above the level of the molten flux), we conclude that they grew

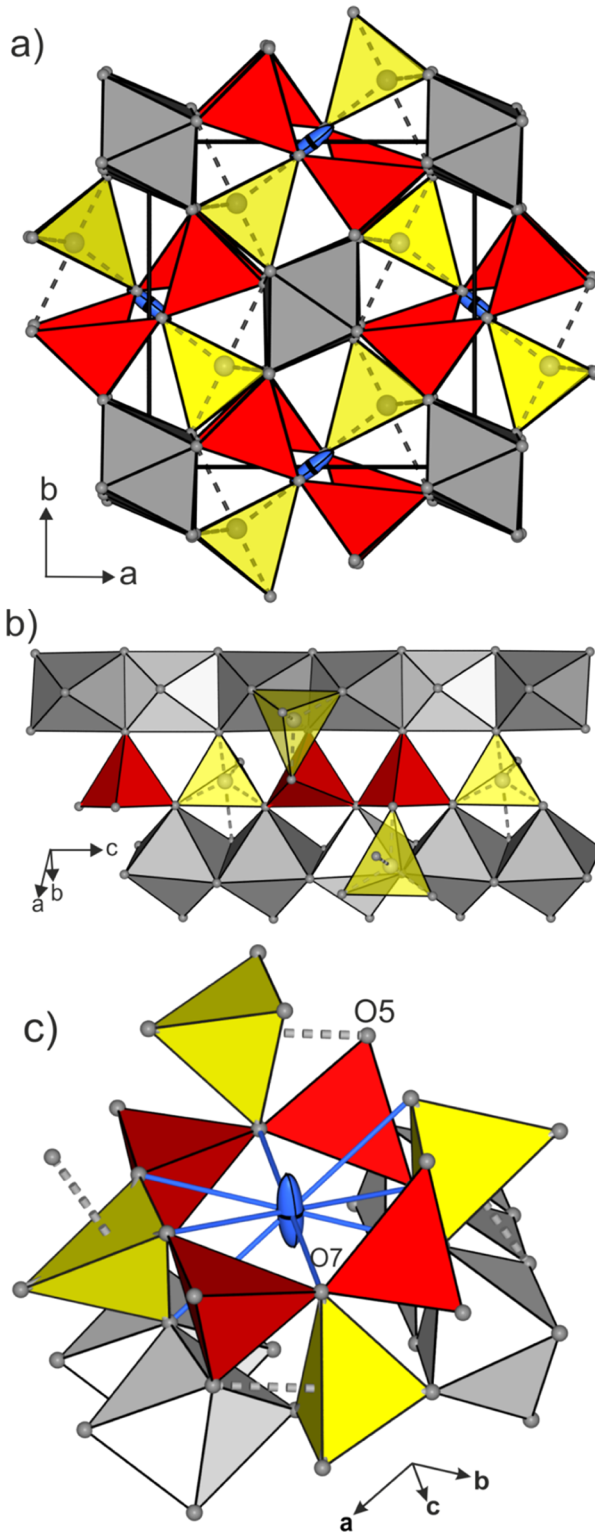
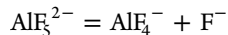


Figure 9. (a) Mullite-type structure of KAl₉O₁₄ comprising AlO₆ octahedra (gray), AlO₄ tetrahedra (red), and Al5O₅ (yellow). Al5O₅ are presented as tetrahedra, with the fifth bond a straight line. (b) Linear edge sharing octahedral chains, comprising Al1O₆ (dark gray) and Al2O₆ (light gray) octahedra connected with inner chain group comprising two tetrahedra Al3O₄ and Al4O₄ (red) and Al5O₅. (c) Thermal ellipsoid of K-atoms (blue) located in the center of cavities with nearly planar arrangement of bonds.

from a vapor phase. Recent studies performed on melts and vapor of K₃AlF₆ reveal possible reactions of this synthesis.

Several authors investigated the phase diagram of the system KF-AlF₃ and reported congruent melting of K₃AlF₆ at 1258,²¹ 1273,²² or 1298 K.²² Mass spectrometric studies above KF-AlF₃ melts²³ suggest that KAlF₄, K₂Al₂F₈, and KF exist as the main vapor phases. By means of the condensation technique, Zhou²⁴ determined that the vapor above pure K₃AlF₆ at 1373 K consists of 12.6 mol % KF and 87.4 mol % KAlF₄ (the amount of K₂Al₂F₈ was considered to be negligible). Raman spectroscopy and vapor pressure studies were not performed on pure K₃AlF₆, but on a molten KF-AlF₃ mixture, and the existence of two equilibria in the melt was proposed:²⁴



The fluoroaluminate species AlF₆³⁻, AlF₅²⁻, and AlF₄⁻^{25,26} may be present in the vapor phase. KAlF₄ is the most promising candidate, as according to Zhou²⁴ it shows the largest abundance and according to Thompson²⁷ significant vapor pressure. To form mullite-type potassium aluminate, a reaction with moisture from the air is required:



As mentioned earlier, the relation between the unit cell of orthorhombic KAl₉O₁₄⁴ and the new monoclinic polymorph is defined by the following transformation: $a_{\text{mon}} = a_{\text{or}} - c_{\text{or}}$, $b_{\text{mon}} = b_{\text{or}}$, $c_{\text{mon}} = 3c_{\text{or}}$. The unit cell volume of the monoclinic polymorph is 3 times larger than the orthorhombic cell. We calculated the X-ray powder diffraction pattern of the new monoclinic superstructure and compared it to the measured powder pattern of the orthorhombic phase.^{4,17} Figure 10 shows

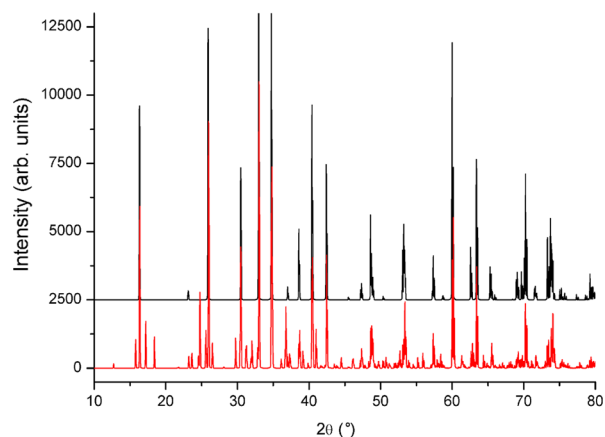


Figure 10. X-ray powder diffraction diagrams (Cu K α 1) of KAl₉O₁₄: (1) orthorhombic polymorph (black);⁴ and (2) calculated powder diagram of the monoclinic superstructure (red).

that the peaks of the orthorhombic phase occur as a substructure pattern in the powder diagram of the monoclinic phase. The differences (superstructure reflections) are rather large and cannot be overlooked, even in powder patterns of lower quality. Therefore, the existence of two distinct polymorphs is highly likely.

As the orthorhombic structure is characterized by disorder, a hypothetical $3 \times a_{\text{or}}$ ordered superstructure was suggested (see Figure 4 in ref 4). Layers of the $3 \times a_{\text{or}}$ superstructure can be found within the monoclinic structure. The monoclinic structure can be assembled from layers of the $3 \times a_{\text{or}}$

superstructure, stacked with a stacking vector of $a_{\text{or}} + c_{\text{or}}$ (which corresponds to a_{mon}). Figure 11 shows a projection

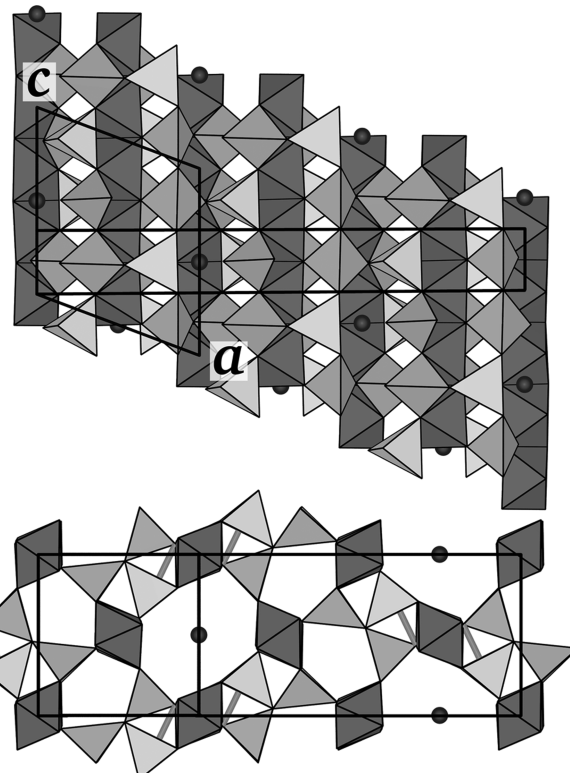


Figure 11. The relation of the basic orthorhombic, the $3 \times a_{\text{or}}$ orthorhombic superstructure, and the monoclinic superstructure. The upper image shows a projection parallel $b_{\text{mon}} (=b_{\text{or}})$. The cell of the $3 \times a_{\text{or}}$ superstructure is shaded in light gray, and shown in projection along c below.

along b , which illustrates the relation of the basic orthorhombic, the $3 \times a_{\text{or}}$ orthorhombic superstructure, and the monoclinic superstructure. The observed twinning as well as the one-dimensional diffuse scattering can be explained in the context of the layers with the $3 \times a_{\text{or}}$ orthorhombic superstructure. A fully ordered stacking sequence with stacking vectors of $(1, 0, 1)$ or $(-1, 0, 1)$ [related to the basic orthorhombic cell] creates twin-related domains of the monoclinic structure. The one-dimensional diffuse scattering proves the existence of disorder. In relation to the basic orthorhombic cell, the diffuse streaks occur at $h \pm 1/3$ (see Figure 5), which is in agreement with stacking faults due to a $3 \times a_{\text{or}}$ superstructure with given stacking vectors.

As discussed earlier, the $l = 3n$ reflections show higher intensities than explained by the structural model comprising the two twin domains only. The additional intensity can be attributed to diffraction from disordered domains, which do not contribute to the $l \neq 3n$ Bragg reflections, but only to the reflections of the basic orthorhombic cell. Considering this model, it cannot be excluded that the basic orthorhombic structure⁴ is actually a $3 \times a_{\text{or}}$ orthorhombic superstructure with random stacking faults, as the diffuse scattering may not be easily visible in powder patterns.

The linear thermal expansion coefficients have been calculated from the lattice parameters, transformed to the basic orthorhombic setting, as determined by single-crystal XRD at room temperature and 1083 K. Their values are: $\alpha(a_{\text{or}})$

$\alpha = 4.0 \times 10^{-6}$, $\alpha(b_{\text{or}}) = 5.8 \times 10^{-6}$, $\alpha(c_{\text{or}}) = 9.5 \times 10^{-6}$, and $\alpha(V) = 19.3 \times 10^{-6} \text{ K}^{-1}$. The anisotropy factor A^{30} was determined to 11.0. As compared to other mullites and mullite-type structures, which exhibit anisotropy factors from 3.8 to 7.8,^{28–30} $\text{KAl}_9\text{O}_{14}$ expands more anisotropically. The common $\alpha(b) > \alpha(c) > \alpha(a)$ pattern of mullites³⁰ is broken by the dominant expansion along c . In $\text{KAl}_9\text{O}_{14}$, the inner chain groups are exclusively trilusters of two tetrahedra and one trigonal bipyramidal (4 + 1 coordination). The additional longer Al5–O5 bond (2.16 Å) of the trigonal bipyramids exhibits a large component in the b -direction (angle Al5–O5 with b is ca. 26°), which may hinder thermal expansion along b and as a result force a larger expansion along c .

■ ASSOCIATED CONTENT

Supporting Information

An X-ray crystallographic file (CIF) for $\text{KAl}_9\text{O}_{14}$. Atomic coordinates and U_{iso} , anisotropic displacement parameters, and selected bond distances for $\text{KAl}_9\text{O}_{14}$ can be found in Tables 2–4 (PDF). Unpolarized Raman spectra of $\text{KAl}_9\text{O}_{14}$ and K- β -alumina in (xy) text format. This material is available free of charge via the Internet at <http://pubs.acs.org>.

■ AUTHOR INFORMATION

Corresponding Author

*E-mail: biljana.lazic@krist.unibe.ch.

Notes

The authors declare no competing financial interest.

■ ACKNOWLEDGMENTS

Financial support for this project has been obtained from the Swiss National Science Foundation under the grant IZ73Z_127961. H.K. acknowledges financial support from the Austrian Science Fund (FWF): J2996-N19. R.L.W. acknowledges support from the Australian Research Council in the form of ARC Discovery grants. We thank Dr. Aleksandar Pacevski, University of Belgrade, for help with SEM/EDX analysis.

■ REFERENCES

- (1) Schneider, H.; Schreuer, J.; Hildmann, B. *J. Eur. Ceram. Soc.* **2008**, *28*, 329.
- (2) Fischer, R. X.; Schneider, H.; Schmücker, M. *Am. Mineral.* **1994**, *79*, 983.
- (3) Schneider, H.; Komarneni, S. *Mullite*; Wiley-VCH: Weinheim, 2005.
- (4) Fischer, R. X.; Schmücker, M.; Angerer, P.; Schneider, H. *Am. Mineral.* **2001**, *86*, 1513.
- (5) Perrotta, A. J.; Young, J. E., Jr. *J. Am. Ceram. Soc.* **1974**, *57*, 405.
- (6) Mazza, D.; Vallino, M. *J. Am. Ceram. Soc.* **1992**, *75*, 1929.
- (7) Elliot, A. G.; Huggins, R. A. *J. Am. Ceram. Soc.* **1975**, *58*, 497.
- (8) Mazza, D.; Ronchetti, S.; Delmastro, A. *Chem. Mater.* **2001**, *13*, 103.
- (9) Angerer, P. Alkalialuminates und Alkaligallate mit Mullitstruktur. Ph.D. Thesis, University of Hannover, 2001.
- (10) Stoe & Cie GmbH. X-Area 1.39; Darmstadt, Germany, 2007.
- (11) Altomare, A.; Cascarano, G.; Giacovazzo, C.; Guagliardi, A.; Burla, M. C.; Polidori, G.; Camalli, M. *J. Appl. Crystallogr.* **1994**, *27*, 435.
- (12) Petricek, V.; Dusek, M.; Palatinus, L. *Jana2006*; Institute of Physics: Praha, Czech Republic, 2006.
- (13) Krüger, H.; Breil, L. *J. Appl. Crystallogr.* **2009**, *42*, 140.
- (14) Horiba Jobin Yvon S.A.S. LABSPEC 5; Longjumeau Cedex, France, 2010.
- (15) Dernier, P. D.; Remeika, J. P. *J. Solid State Chem.* **1976**, *17*, 245.
- (16) Xu, J.-A.; Huang, E.; Lin, J.-F.; Xu, J. *Y. Am. Mineral.* **1995**, *80*, 1157.
- (17) Brandenburg, K.; Putz, H. DIAMOND 3.2; Crystal Impact GbR: Germany, 2005.
- (18) Robinson, K.; Gibbs, G. V.; Ribbe, P. H. *Science* **1971**, *172*, 567.
- (19) Wang, Z.; Shi, G. P.; Sun, X.; Hou, X. Q. *Key Eng. Mater.* **2008**, *368–372*, 710.
- (20) Hashimoto, S.; Yamaguchi, A. *J. Ceram. Soc. Jpn.* **2004**, *112*, 104.
- (21) Phillips, B.; Warshaw, C. M.; Mockrin, I. *J. Am. Ceram. Soc.* **1966**, *49*, 631.
- (22) Holm, B. J. Ph.D. Thesis, University of Trondheim, Norway, 1969.
- (23) Kolosov, E. N.; Sidrov, L. N.; Voloronin, G. F. *Russ. J. Phys. Chem.* **1971**, *45*, 1548.
- (24) Zhou, H. Thermodynamic studies of cryolite based melts: vapor pressure measurements, model calculations. Ph.D. Thesis, University of Trondheim, Norway, 1991.
- (25) Robert, E.; Olsen, J. E.; Gilbert, B.; Ostvold, T. *Acta Chem. Scand.* **1997**, *51*, 397.
- (26) Tixhon, E.; Robert, E.; Gilbert, B. *Appl. Spectrosc.* **1994**, *48*, 1477.
- (27) Thompson, W. T.; Goad, D. G. W. *Can. J. Chem.* **1976**, *54*, 3342.
- (28) Brunauer, G.; Frey, F.; Boysen, H.; Schneider, H. *J. Eur. Ceram. Soc.* **2001**, *21*, 2563.
- (29) Gesing, T. M.; Schowalter, M.; Weidenthaler, C.; Murshed, M. M.; Nenert, G.; Mendive, C. B.; Curti, M.; Rosenauer, A.; Buhl, J.-C.; Schneider, H.; Fischer, R. X. *J. Mater. Chem.* **2012**, *22*, 18814.
- (30) Schneider, H.; Eberhard, E. *J. Am. Ceram. Soc.* **1990**, *73*, 2073.